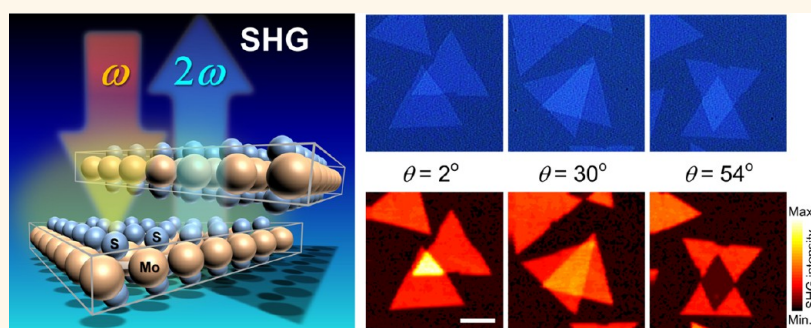


# Second Harmonic Generation from Artificially Stacked Transition Metal Dichalcogenide Twisted Bilayers

Wei-Ting Hsu,<sup>†</sup> Zi-Ang Zhao,<sup>†</sup> Lain-Jong Li,<sup>†,§</sup> Chang-Hsiao Chen,<sup>‡</sup> Ming-Hui Chiu,<sup>‡</sup> Pi-Shan Chang,<sup>†</sup> Yi-Chia Chou,<sup>†</sup> and Wen-Hao Chang<sup>†,\*</sup>

<sup>†</sup>Department of Electrophysics, National Chiao Tung University, Hsinchu 30010, Taiwan, <sup>‡</sup>Institute of Atomic and Molecular Sciences, Academia Sinica, Taipei 10617, Taiwan, and <sup>§</sup>Department of Medical Research, China Medical University Hospital, Taichung 40402, Taiwan

## ABSTRACT



Optical second harmonic generation (SHG) is known as a sensitive probe to the crystalline symmetry of few-layer transition metal dichalcogenides (TMDs). Layer-number dependent and polarization resolved SHG have been observed for the special case of Bernal stacked few-layer TMDs, but it remains largely unexplored for structures deviated from this ideal stacking order. Here we report on the SHG from homo- and heterostructural TMD bilayers formed by artificial stacking with an arbitrary stacking angle. The SHG from the twisted bilayers is a coherent superposition of the SH fields from the individual layers, with a phase difference depending on the stacking angle. Such an interference effect is insensitive to the constituent layered materials and thus applicable to hetero-stacked bilayers. A proof-of-concept demonstration of using the SHG to probe the domain boundary and crystal polarity of mirror twins formed in chemically grown TMDs is also presented. We show here that the SHG is an efficient, sensitive, and nondestructive characterization for the stacking orientation, crystal polarity, and domain boundary of van der Waals heterostructures made of noncentrosymmetric layered materials.

**KEYWORDS:** transition metal dichalcogenide · MoS<sub>2</sub> · second harmonic generation · SHG · two-dimensional layered materials · artificial stacking

Few-layer group VI transition metal dichalcogenides (TMDs), such as MX<sub>2</sub> (M = Mo, W; X = S, Se), are semiconducting layered materials, exhibiting fascinating layer-number dependent electronic and optical properties,<sup>1</sup> which are sensitive to the underlying crystal symmetry and differ greatly from their bulk counterparts. For instance, single-layer molybdenum disulfide (MoS<sub>2</sub>) is known as a direct-gap semiconductor with broken inversion symmetry in its crystalline structure,<sup>1–3</sup> which can generate strong valley dependent polarizations by helical lights.<sup>4–6</sup> Bilayer MoS<sub>2</sub>, on the other hand, has vanished valley polarization due to the restoration of crystal

inversion symmetry.<sup>5,6</sup> The presence or the absence of inversion symmetry in few-layer TMDs also manifests itself in their second-order optical nonlinearity. Intense and layer-number dependent optical second harmonic generation (SHG) have been observed in few-layer TMDs,<sup>7–11</sup> owing to the nonvanished second-order nonlinearity associated with the broken inversion symmetry in flakes with odd number of layers. However, such layer-number dependent properties are preserved only when the few-layer TMDs are Bernal stacked.<sup>7,9,10</sup> Unlike those prepared by exfoliation from nature crystals, the few-layer TMDs<sup>8</sup> or hexagonal boron nitride (h-BN)<sup>11</sup> grown by chemical vapor

\* Address correspondence to whchang@mail.nctu.edu.tw.

Received for review January 14, 2014 and accepted February 25, 2014.

Published online February 25, 2014  
10.1021/nn500228r

© 2014 American Chemical Society

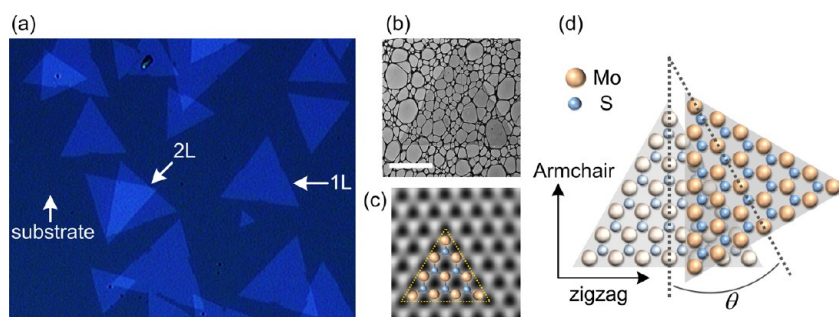


**Figure 1.** (a) An optical microscopy image of the artificially stacked MoS<sub>2</sub> bilayers. Monolayer (1L), bilayer (2L), and substrate regions are indicated by arrows. (b) A low-magnification TEM image for a triangular MoS<sub>2</sub> monolayer flake. The scale bar is 5  $\mu\text{m}$ . (c) The FFT filtered HR-TEM image of the MoS<sub>2</sub> flake shown in (b). The hexagonal lattice structure is clearly observed, with brighter spots corresponding to the Mo sites. (d) A schematic showing the lattice structure of an artificially stacked MoS<sub>2</sub> bilayer with a stacking angle  $\theta$ .

deposition (CVD) may deviate from this ideal stacking order with interlayer rotations, displacements, or even stacking faults. The structure–property relationships in twisted bilayer graphene have been investigated intensively recently;<sup>12–15</sup> however, they remain largely unexplored for twisted bilayer TMDs.

Furthermore, recent advances in isolating and subsequent restacking of heterogeneous layered materials, including graphene, h-BN, and TMDs, have opened up a new research direction for exploring new properties and functionalities of artificial materials for versatile applications.<sup>16</sup> The success of these van der Waals hybrid materials has manifested itself in flexible photovoltaic devices<sup>17</sup> and field-effect tunneling transistors.<sup>18</sup> Vertical stacking of TMDs homo- and hetero-structures with precise control of twist angles would create new materials with a tailored interlayer coupling that is strongly stacking orientation dependent.<sup>13,14,19,20</sup> Therefore, an efficient and noninvasive characterization tool for identifying the stacking angle is desirable. In this context, the SHG appears as a promising technique, since the second harmonic (SH) response is a sensitive probe to the underlying crystal-line symmetry and orientation. The SH microscopy has been proven to be useful for identifying the odd/even number of layers<sup>7,9,10</sup> and probing the crystallographic axis<sup>8–11</sup> in few-layer TMDs and h-BN. However, the stacking angle dependence of the SHG from homo- and hetero-stacked TMD twisted bilayers has yet to be established.

In this work, we investigate the SH response of artificially stacked TMDs bilayers with an arbitrary stacking angle. We first start from the prototypical homo-stacked MoS<sub>2</sub>/MoS<sub>2</sub> bilayers and demonstrate that the SHG from the twisted bilayers is a coherent superposition of the SH fields from the constituent monolayers, with a phase difference depending on the stacking angle. The resulting intensity and polarization of the SHG as a function of the stacking angle can thus be established. We further extend the study to hetero-stacked WSe<sub>2</sub>/MoS<sub>2</sub> and WSe<sub>2</sub>/WS<sub>2</sub> bilayers and show that the same idea is applicable and insensitive to the

constituent layered materials. Finally, a proof-of-concept demonstration of using the SH microscopy to probe structural defects in CVD-grown TMDs, such as the domain boundary and crystal polarity of mirror twins, is presented.

## RESULTS AND DISCUSSION

Figure 1a shows an optical microscopy image of the artificially stacked MoS<sub>2</sub> bilayers. Monolayer MoS<sub>2</sub> flakes were first synthesized by CVD on sapphire substrates.<sup>21</sup> The artificially stacked MoS<sub>2</sub> bilayers were then fabricated by transferring the as-grown monolayer flakes onto another substrate with monolayer flakes already formed thereon (see Methods). The CVD-synthesized MoS<sub>2</sub> flakes are mostly in triangular shape with a typical side length of around  $\sim 10\ \mu\text{m}$ . According to high-resolution transmission electron microscopy (HR-TEM) and optical (Photoluminescence and Raman) characterizations (see Supporting Information), these triangular MoS<sub>2</sub> flakes are monolayer thick and single crystalline with edges along the zigzag direction (Figure 1b,c). Therefore, the crystallographic twist angles of the MoS<sub>2</sub> bilayers (Figure 1d) can be determined directly by the relative orientation between the two constituent triangular flakes observed in optical microscopy images.

To illustrate how the stacking orientation affects the optical SHG, we select here two representative stacking orientations in nearly parallel ( $\theta \approx 0^\circ$ ) and antiparallel ( $\theta \approx 60^\circ$ ) configurations. Figure 2a,b shows the optical microscopy images of the two stacking configurations. The corresponding spatial mappings of SH intensity from individual monolayer MoS<sub>2</sub> flakes and the stacking regions are displayed in Figure 2c,d. In this experiment, we measured the total SH power, which is independent of the polarization direction of the incident laser field with respect to the crystallographic axis. For the case of antiparallel stacking (Figure 2c), the SH intensity from each MoS<sub>2</sub> flake is quite uniform, except for the stacking region, where the SH intensity is strongly suppressed. It is well-known that the SHG signal occurs (vanishes) in materials with the absence

(presence) of inversion symmetry. Monolayer MoS<sub>2</sub> crystal belongs to the  $D_{3h}$  point group with broken inversion symmetry and thus allows strong SHG. For MoS<sub>2</sub> bilayers exfoliated from bulk crystal with the Bernal ( $2H$ ) stacking order, the crystal belongs to the  $D_{3d}$  point group with inversion symmetry and hence vanishes the SH response. The strongly suppressed SH

response in the stacking region shown in Figure 2c indicates that the underlying crystal symmetry is close to the Bernal stacked bilayer. On the contrary, as shown in Figure 2d for the case of nearly parallel stacking, an enhanced SH intensity can be observed in the stacking region. The SH intensity is about  $\sim 3.2$  times stronger than that of individual monolayers. This demonstrates that the SH response is sensitive to the stacking orientation, which cannot be observed in few-layer MoS<sub>2</sub> exfoliated from bulk crystal with the ideal Bernal stacking.

The underlying crystal symmetry and crystallographic orientation of individual monolayer MoS<sub>2</sub> flakes and the stacking regions can be further examined by the polarization-resolved SHG. We select here a particular bilayer with a stacking angle of  $\theta \cong 25^\circ$  between flakes 1 and 2 (Figure 3a). The SHG experiment is performed in a back-reflection geometry using a pump laser normally incident on the sample (Figure 3b). The incident pump laser is linearly polarized along the  $x$  direction, which is initially aligned with the armchair direction of the flake 1 (Figure 3c). For the monolayer MoS<sub>2</sub> crystal with a three-fold rotational symmetry, the SH response with a polarization parallel (perpendicular) to the incident laser polarization is known to exhibit a six-fold rotational symmetry, with a SH intensity varies as  $I_{\parallel} \propto \cos^2 3\varphi$  ( $I_{\perp} \propto \sin^2 3\varphi$ ),<sup>8–11,22</sup> where  $\varphi$  is the azimuthal angle between the incident laser polarization and the armchair direction. The SH

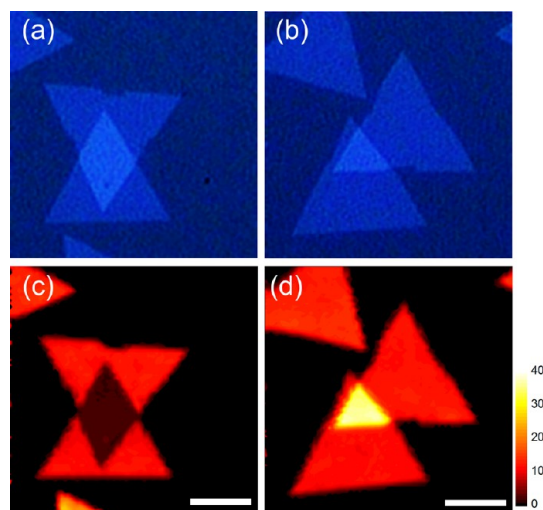


**Figure 2.** (a and b) Optical microscopy images for stacked MoS<sub>2</sub> bilayers with a stacking angle of (a)  $\theta \cong 60^\circ$  and (b)  $\theta \cong 0^\circ$ . (c and d) The corresponding false color-coded SH intensity obtained by pixel-to-pixel spatial mappings of flakes in (a) and (b). The scale bars are 5  $\mu\text{m}$ .

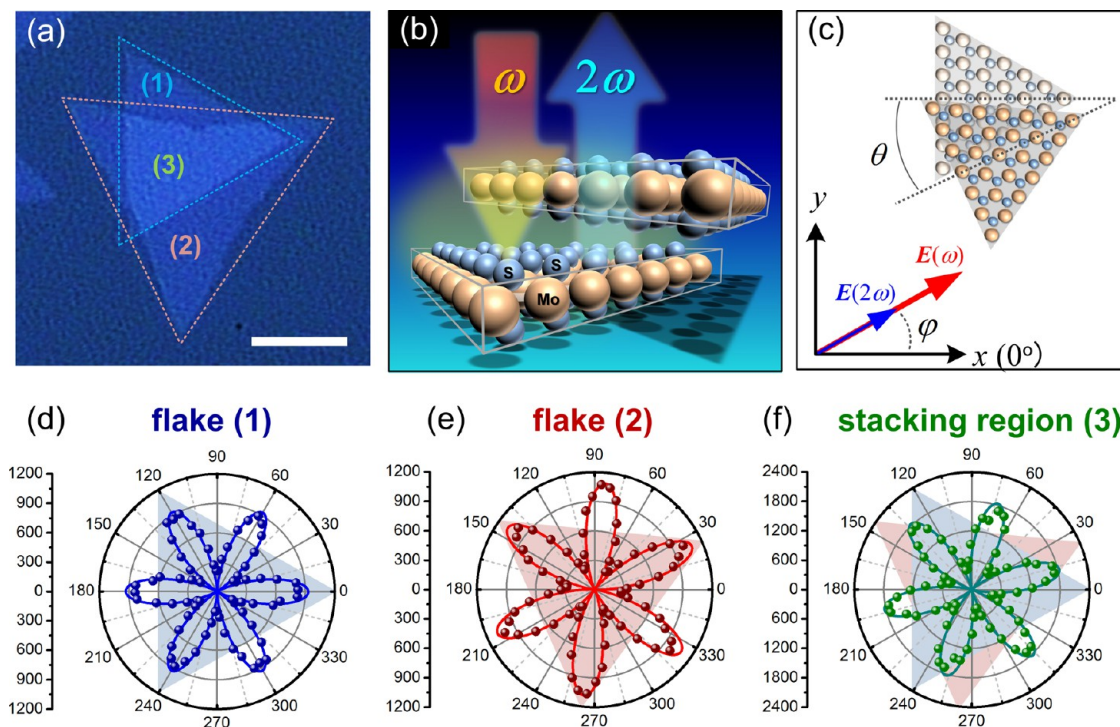


**Figure 3.** (a) The optical microscopy image of a particular MoS<sub>2</sub> bilayer with a stacking angle of  $\theta \cong 25^\circ$ . The scale is 5  $\mu\text{m}$ . (b and c) Schematics showing (b) the measurement geometry and (c) the polarization directions of the incident laser and the measured SHG. The azimuthal angle  $\varphi$  defines the angle between the laser polarization and the  $x$ -axis, which is aligned with the armchair direction of the flake (1). (d–f) Polar plots of the polarization-resolved SH intensity as a function of azimuthal angle  $\varphi$  measured from (d) the monolayer region (1), (e) the monolayer region (2), and (f) the stacking region (3).



response thus shows an intensity maximum when the incident laser polarization aligns with the armchair (zigzag) direction for the parallel (perpendicular) polarization configuration.<sup>8–10</sup> As shown in Figure 3d,e, the polarization-resolved SHG of individual flake (measured under the parallel polarization configuration) shows a six-petal pattern, with petals lying along the perpendicular bisectors of each flake. This also agrees with our TEM analysis, where the perpendicular bisectors (edges) of the MoS<sub>2</sub> triangles are aligned with the armchair (zigzag) directions. Interestingly, the SH light from the stacking region also show a six-petal polarization pattern (Figure 3f), but with petals lying along a direction between the two nearest perpendicular bisectors of flakes 1 and 2. This clearly indicates that the SHG from the stacking region is not contributed independently from individual flakes.

The SH response in the artificially stacked MoS<sub>2</sub> bilayers can be modeled as two electrically decoupled layers of atomically thin sheet dipole moments driven coherently by the fundamental laser field.<sup>10</sup> The linearly polarized fundamental laser field generates linearly polarized SH fields from each layer, with a polarization direction determined by the angle between laser polarization and the respective armchair direction of each layer. The SH fields generated from the two layers then interfere coherently with a phase difference depending on the stacking angle. The resulting polarization of SHG from the stacking region thus retains the six-fold rotational symmetry, but with petals lying between the two flakes. Furthermore, the coherent superposition of SH fields can be either constructive or destructive, leading to an enhanced or suppressed SH intensity in the stacking region. This simple model has been employed to explain some experimental signatures of SHG observed in CVD-synthesized few-layer MoS<sub>2</sub><sup>8</sup> and h-BN.<sup>11</sup> Kumar *et al.* found that the bilayer regions in the central area of MoS<sub>2</sub> triangles have a stronger SH intensity as compared with monolayer regions,<sup>8</sup> indicating that the MoS<sub>2</sub> bilayer is not in the 2H-stacking order. Kim *et al.* found that h-BN bilayers exhibit a stronger (weaker) SH intensity in the AB (AA') stacking configuration,<sup>11</sup> and the SH intensity in the AB stacking regions is ~4 times stronger than that in monolayer regions, in good agreement with the interference model described above.

Here we provide a full description of the model for SHG in bilayers TMDs with an arbitrary stacking angle. Let us consider the stacked bilayers as two electrically decoupled layers, and first neglect the propagating effects of electromagnetic waves in these atomically thin layers. If the laser electric field  $\vec{E}(\omega)$  makes an angle of  $\varphi_1$  ( $\varphi_2$ ) with respect to the armchair direction of flake 1 (flake 2), the generated SH electric field  $\vec{E}_1(2\omega)$  [ $\vec{E}_2(2\omega)$ ] from the flake 1 (flake 2) is then  $3\varphi_1$  ( $3\varphi_2$ ) away from the laser polarization (Figure 4a). The total

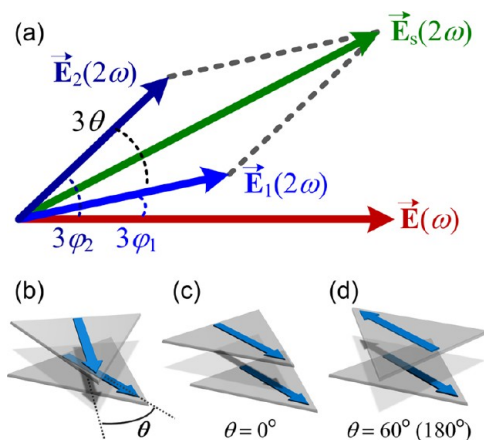


**Figure 4.** (a) A schematic for illustrating the vector superposition of the SH electric fields, where  $\vec{E}(\omega)$  is the electric field of the fundamental light,  $\vec{E}_1(2\omega)$  [ $\vec{E}_2(2\omega)$ ] is the SH electric field from the flake 1 (flake 2), and  $\vec{E}_s(2\omega)$  is the resulting SH electric field from the stacking region. (b–d) Schematics for stacked bilayers with (b) an arbitrary stacking angle  $\theta$ , (c)  $\theta = 0^\circ$ , and (d)  $\theta = 60^\circ$  (or  $\theta = 180^\circ$ ).

SH electric field  $\vec{E}_s(2\omega)$  in the stacking region can then be obtained by a vector superposition:  $\vec{E}_s(2\omega) = \vec{E}_1(2\omega) + \vec{E}_2(2\omega)$ . The total SH intensity in the stacking region is proportional to  $|\vec{E}_s(2\omega)|^2$ , which can be expressed as

$$I_s(\theta) = I_1 + I_2 + 2\sqrt{I_1 I_2} \cos 3\theta \quad (1)$$

where  $I_s$ ,  $I_1$ , and  $I_2$  stand for the SH intensity in the stacking region, the monolayer flake 1, and flake 2, respectively; and  $\theta = \varphi_1 - \varphi_2$  is the stacking angle, which is defined as the angle between two nearest perpendicular bisectors of the two triangular flakes (Figure 4b). That is,  $\theta = 0^\circ$  yields a completely constructive interference, whereas  $\theta = 60^\circ$  yields a completely destructive interference of SH fields (Figure 4c,d). Although the artificial stack with  $\theta = 60^\circ$  is analogous to natural MoS<sub>2</sub> bilayer with  $D_{3d}^2$  symmetry, it should be noted that the artificial stack might present lateral displacements between the two layers, making the  $\theta = 60^\circ$  stacking not truly in the Bernal stacking. However, such a lateral displacement is unable to resolve by the SHG technique, since the optical wavelength is much longer than the lateral misalignment of less than one lattice constant.

We have examined the SH response of the artificially stacked bilayers with different stacking angles distributed in the range of  $0^\circ \leq \theta < 60^\circ$ . Figure 5a shows the optical microscopy images of a series of MoS<sub>2</sub> bilayers with different stacking angles. The corresponding SH intensity mappings are displayed in the same color scale in Figure 5b. It is clear that the SH intensity in the bilayer region changes dramatically with the stacking angle. According to (1), the stacking angle dependent SH intensity should vary as  $\cos 3\theta$  and from  $I_s(0^\circ) = 4I_0$  (fully constructive) to  $I_s(60^\circ) = 0$  (fully destructive) if  $I_1 = I_2 = I_0$ , i.e., the SH intensities from different flakes are the

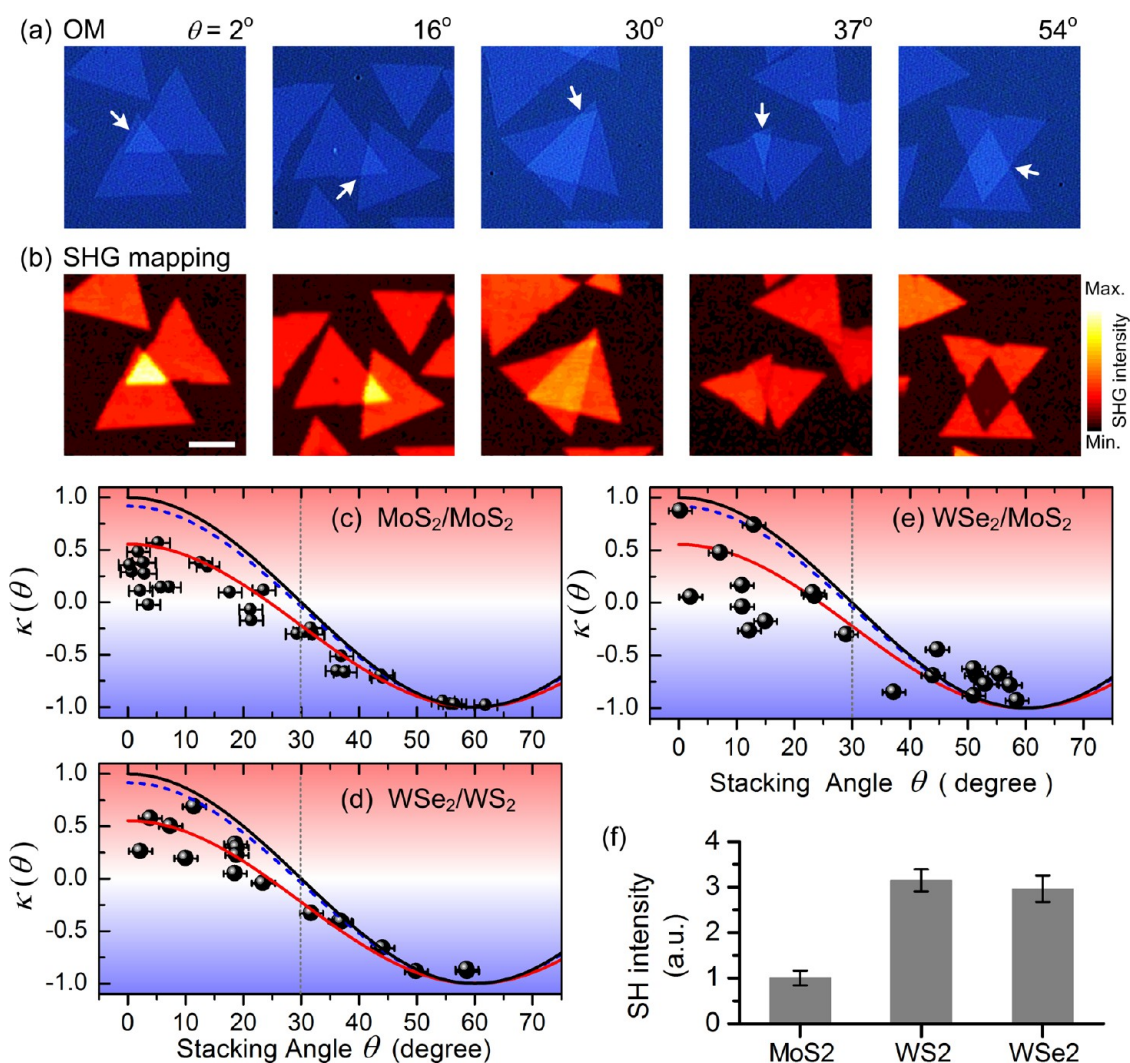


**Figure 5.** (a) Optical microscopy images for a series of MoS<sub>2</sub> bilayers with a stacking angle distributed from  $\theta = 0^\circ$  to  $60^\circ$ . (b) The corresponding false color-coded SH intensity mappings of flakes shown in (a). The scale bar is  $5\ \mu\text{m}$ . (c–e) The measured angular dependence of  $\kappa(\theta)$  for (c) homogeneous MoS<sub>2</sub>/MoS<sub>2</sub> bilayers, (d) heterogeneous WSe<sub>2</sub>/WS<sub>2</sub> bilayers, and (e) heterogeneous WSe<sub>2</sub>/MoS<sub>2</sub> bilayers. Curves are calculated  $\kappa(\theta)$ : black solid curves,  $\kappa(\theta) = \cos 3\theta$ ; red, (blue dashed) curves, calculations considering the propagation effects of electromagnetic waves with (without) including material absorption. Symbols are data points collected from all the investigated bilayers. (f) The measured SH intensities for MoS<sub>2</sub>, WS<sub>2</sub>, and WSe<sub>2</sub> monolayers.

same. However, such an angular dependence could be screened by the presence of SH intensity variation ( $\sim 10\text{--}15\%$ ) among different flakes. Therefore, we define here a dimensionless parameter  $\kappa(\theta) \equiv (I_s - I_1 - I_2)/2(I_1 I_2)^{1/2}$  and then examine its angular dependence. In this way, the intensity variation among different flakes can be normalized and, in principle, the angular dependence of  $\kappa(\theta) = \cos 3\theta$  should be recovered. It should be noted that the value of  $\cos 3\theta$  changes sign at  $\theta = 30^\circ$ . A positive (negative)  $\kappa(\theta)$  value indicates a constructive (destructive) interference and, hence, an enhanced (suppressed) SH intensity in the stacking region, *i.e.*,  $I_s > I_1 + I_2$  ( $I_s < I_1 + I_2$ ). As shown in Figure 5c, the extracted  $\kappa(\theta)$  for the homo-stacked MoS<sub>2</sub>/MoS<sub>2</sub> bilayers follows closely to  $\cos 3\theta$  (black curve), in agreement with the simple model prediction. However, the measured interference contrast is

somewhat lower than the simple model prediction; *i.e.*, the experimental data always lies below the  $\cos 3\theta$  dependence. Moreover, the extracted  $\kappa(\theta)$  values also change sign at  $\theta < 30^\circ$ . To account for the reduced interference contrast, we have further included the propagating effects of electromagnetic waves through the TMD layers and the underlying substrate. The phase shift, absorption, and reflection of both the fundamental laser field and the SH fields in the TMD layers and at the adjacent interfaces have been taken into account (see Supporting Information for detail). After including the propagating effects of electromagnetic waves, the calculated SH response (red curve) reproduces the measured  $\kappa(\theta)$  very well. In this calculation, we found that the optical absorption of the SH light by the upper TMD layer plays a key role, leading to incomplete interferences. This can be verified from a

calculation without including the material absorption, where only a minor change in the interference contrast caused by the multilayer reflections. The absorption coefficient at the SH wavelength used in this calculation was obtained by differential reflectance measurements (see Methods). For monolayer MoS<sub>2</sub>, the absorbance is estimated to be  $\sim 12.9\%$  at wavelength  $\lambda = 405$  nm, corresponding to an absorption coefficient of  $\alpha \approx 2.1 \times 10^6 \text{ cm}^{-1}$  (see Supporting Information). This value is comparable to the reported values in literature for bulk MoS<sub>2</sub>.<sup>23</sup>

On the basis of the understanding of MoS<sub>2</sub>/MoS<sub>2</sub> homo-stacked bilayers, we have further extended the study to hetero-stacked bilayers. The stacking angle dependences of  $\kappa(\theta)$  extracted from selected WSe<sub>2</sub>/WS<sub>2</sub> and WSe<sub>2</sub>/MoS<sub>2</sub> hetero-stacked bilayers are shown in Figure 5, panels d and e, respectively. In both cases, the model including the propagation effects of electromagnetic waves also reproduces the experimental data very well. According to the measured differential reflectance spectra of monolayer WSe<sub>2</sub> and WS<sub>2</sub>, the absorption coefficient at the SH wavelength is nearly the same as the monolayer MoS<sub>2</sub> (see Supporting Information). Therefore, the model predictions for the homo- and hetero-stacked TMD bilayers are expected to be similar, regardless of the constituent layered materials. However, we noted that the measured  $\kappa(\theta)$  for the WSe<sub>2</sub>/MoS<sub>2</sub> bilayers is more scattered (Figure 5e). This might be due to the large difference between the SH efficiencies of MoS<sub>2</sub> and WSe<sub>2</sub> monolayers. The SH intensity of monolayer MoS<sub>2</sub> is about 3 times weaker than that of WSe<sub>2</sub> and WS<sub>2</sub> (Figure 5f), which could lead to incomplete interference and more scattered data. Nonetheless, our results demonstrate that the SHG is capable of probing the underlying symmetry of stacked van der Waals heterostructures made of noncentrosymmetric layered materials.

From the measured  $\kappa(\theta)$  for the homo- and hetero-stacked TMD bilayers, it is also clear that all the triangular TMD monolayers are of the same crystal polarity, *i.e.*, either the transition-metal-polar (Mo, W) or the chalcogen-polar (S, Se), rather than a mixture of both polarities. As has been mentioned above, monolayer TMD crystals exhibit a three-fold rotational symmetry, while the polarization-resolved SH intensity has a six-fold rotational symmetry, since a phase shift of  $\pi$  in the SH field  $\vec{E}(2\omega)$  cannot be distinguished by the measurements of the SH intensity  $|\vec{E}(2\omega)|^2$ . In the artificially stacked TMD bilayers, the stacking angle dependent SH intensity becomes electric-field-resolved due to the interference effect. If the bilayers are made of two TMD monolayers with opposite polarity, the resulting stacking angle dependence will be  $\kappa(\theta) = \sin 3\theta$ . The invariably observed  $\kappa(\theta) = \cos 3\theta$  for all the homo- and hetero-stacked bilayers indicates that all the investigated triangular monolayers are

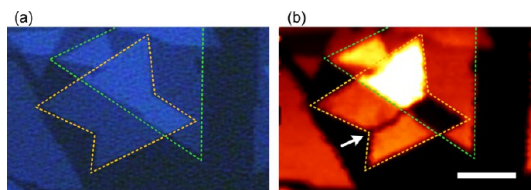


**Figure 6.** (a) An optical microscopy image for a triangular MoS<sub>2</sub> monolayer overlapped with a butterfly-shaped MoS<sub>2</sub> monolayer. (b) The corresponding false color-coded SH intensity obtained by pixel-to-pixel spatial mappings of flakes in (a). The butterfly-shaped MoS<sub>2</sub> monolayer consists of two mirror-twin domains with a twin boundary located at the intersection of the two wings (indicated by arrow).

single-domain with the same crystal polarity. According to the HR-TEM study, our MoS<sub>2</sub> triangular flakes are terminated by Mo-polar zigzag edges, implying that the investigated WS<sub>2</sub> and WSe<sub>2</sub> triangular flakes also have W-polar zigzag edges.

Since the SHG is crystal-orientation-dependent, the SH microscopy in principle is capable of probing the crystallographic axes and grain boundaries of TMD films, especially for tilted grains in polycrystalline aggregates or continuous sheets formed during CVD growths. Notably, however, the intensity-resolved SH microscopy is unable to distinguish the crystal orientations of mirror twins formed by two domains with a relative in-plane rotation of 180°. By laying down a monolayer TMD with known crystal polarity on top of mirror twins, the crystal orientation becomes visualized due to the electric-field resolved interference effect. A proof-of-concept demonstration for the characterization of mirror twins is shown in Figure 6. Let us focus on the butterfly-shaped and the triangular MoS<sub>2</sub> monolayers highlighted by the dotted lines. In the stacking region, the SH intensity shows a strong contrast between the two wings of the butterfly-shaped monolayer, indicating that it consists of two mirror-twin domains, from which the SH fields interfere constructively and destructively with that from the triangular MoS<sub>2</sub> monolayer. The mirror twin boundary in the monolayer region is also visualized for the first time by the SH microscopy, as indicated by the arrow near the intersection between the two wings (Figure 6b). Since the SH dipole moments generated in the mirror twins are completely out of phase, the SH response should vanish at the mirror twin boundary, resulting in a strongly suppressed SH intensity.

## CONCLUSIONS

We have investigated the SHG from artificially stacked TMD bilayers with arbitrary stacking angles. The SHG from the twisted bilayers is a coherent superposition of the SH fields from the individual layers, with a phase difference depending on the stacking angle. Such an interference effect is insensitive to the constituent layered materials and thus applicable to hetero-stacked bilayers. The intensity and the polarization



of SHG as a function of the stacking angle have been established. A proof-of-concept demonstration of using the SHG to probe the domain boundary and crystal polarity of mirror twins formed in chemically grown TMDs is also presented. We have demonstrated

here that the SHG is an efficient, sensitive, and non-destructive characterization for the stacking orientation, crystal polarity, and domain boundary of van der Waals heterostructures made of noncentrosymmetric layered materials.

## METHODS

**Growth of Monolayer TMDs.** High-crystal-quality monolayers MoS<sub>2</sub>, WSe<sub>2</sub>, and WS<sub>2</sub> were synthesized on sapphire substrates by chemical vapor deposition (CVD) in a horizontal hot-wall chamber. The detailed fabrication procedures can be found elsewhere.<sup>21,24,25</sup> High purity MoO<sub>3</sub> (99%, Aldrich), WO<sub>3</sub> (99%, Alfa), Se and S powders (99.5%, Alfa) were used as initial reactants. The MoS<sub>2</sub> and WS<sub>2</sub> samples were obtained by annealing at 650 and 800 °C for 5 min with a heating rate of 15 °C/min and Ar flow at ambient pressure. For the synthesis of WSe<sub>2</sub>, the center heating zone with the WO<sub>3</sub> powders was heated to 925 °C, while the Se powders placed at the upper stream side were maintained at 270 °C. The WSe<sub>2</sub> samples were obtained by placing the substrate at the downstream side using an Ar/H<sub>2</sub> flowing gas at 1 Torr for 15 min.

**Transfer of Monolayer TMD To Form Bilayers.** The artificially stacked TMD bilayers were fabricated by transferring monolayer TMD flakes onto another as-grown monolayer TMD formed on a sapphire substrate. For MoS<sub>2</sub> transfer, a layer of poly(methylmethacrylate) (PMMA) (950K A4) was first coated on the monolayer MoS<sub>2</sub> flakes as a transfer supporting layer by spin-coating (step 1, 500 rpm for 10 s; step 2, 3000 rpm for 60 s), followed by baking at 100 °C for 60 min. Then the PMMA-capped MoS<sub>2</sub> was exfoliated from the sapphire substrate in a 2 M NaOH solution at 100 °C for 60 min. After dilution of etchant and residues in deionized water, the PMMA-capped monolayer MoS<sub>2</sub> was transferred onto another as-grown MoS<sub>2</sub> sample, followed by the removal of PMMA film using acetone.<sup>26</sup> Finally, the sample was cleaned by isopropyl alcohol and deionized water. According to the atomic force microscopy (AFM) analyses (Supporting Information), the thickness of MoS<sub>2</sub> monolayer (bilayer) is 0.65 nm (1.3 nm). However, we noted that the PMMA cannot be completely removed by using acetone only. To avoid PMMA contamination in the interlayer region, the PMMA layer was always kept on top of the MoS<sub>2</sub> layers during the transfer process. In this way, the PMMA residues will be mostly residing on the TMD surface. After 300 °C annealing in Ar/H<sub>2</sub> gas flow for 4 h, these PMMA residues can be completely removed. We have also compared SHG from the stacked bilayers with and without thermal annealing. The measured SHG behavior is basically the same. This indicated that the surface PMMA residues have negligible effect on the interlayer coupling of SHG. All the data presented in this work are obtained from samples without thermal annealing.

**Optical Measurements.** The SHG measurements were performed in a homemade microscopy system. The fundamental laser field was provided by a mode-locked Ti:sapphire laser at a wavelength of 810 nm with a pulse width of ~150 fs and a repetition rate of 80 MHz. The laser pulse was focused to a spot size of ~1.1 μm on the sample by a 100× objective lens. The generated SH light was sent to a 0.75 m monochromator and detected by a nitrogen-cooled CCD camera. For spatial mapping of SH intensity, the sample was mounted on a fast motorized x–y stage with a step of 0.25 μm. For polarization-resolved SHG, the sample was rotated by a motorized rotational stage with a step of 5°. The linear polarizations of the fundamental and the SH light were selected and analyzed by individual polarizers and half-wave plates. According to the measured SH intensity, we estimated that the magnitude of the second-order susceptibility  $\chi^{(2)}$  (bulk value) of our CVD-grown MoS<sub>2</sub> monolayer is about  $\chi^{(2)} = 1.5 \times 10^{-10}$  m/V. Although the absolute  $\chi^{(2)}$  value depends sensitively on the experimental conditions (such as the laser wavelength, spot size, pulse width/shape and the collected solid angle), the

deduced  $\chi^{(2)}$  value is very close to the reported value for MoS<sub>2</sub> monolayers prepared by exfoliation from natural crystals.<sup>9,10</sup> For differential reflectance measurements, the apparatus are the same as the SHG measurements, except that the light source was replaced by a fiber-coupled tungsten-halogen lamp.

**Conflict of Interest:** The authors declare no competing financial interest.

**Acknowledgment.** This work was supported in part by the National Science Council of Taiwan under Grant Nos. NSC101-2628-M-009-002-MY3 and NSC102-2119-M-001-005-MY3. W.-H.C. acknowledges the supports from the Center for Interdisciplinary Science under the MOE-ATU project for NCTU. L.-J.L. acknowledges the supports from the Academia Sinica (IAMS and Nano program).

**Supporting Information Available:** AFM analyses and optical characterizations, including Raman, PL and differential reflectance measurements for identifying the number of layers and material quality; determination of the absorption coefficient from the differential reflectance spectra; the effects of multi-layer reflections and absorptions on the SHG; the second-order susceptibility  $\chi^{(2)}$  for bilayers; and the wavelength dependent SHG. This material is available free of charge via the Internet at <http://pubs.acs.org>.

## REFERENCES AND NOTES

- Wang, Q. H.; Kalantar-Zadeh, K.; Kis, A.; Coleman, J. N.; Strano, M. S. Electronics and Optoelectronics of Two-Dimensional Transition Metal Dichalcogenides. *Nat. Nanotechnol.* **2012**, *7*, 699.
- Mak, K. F.; Lee, C.; Hone, J.; Shan, J.; Heinz, T. F. Atomically Thin MoS<sub>2</sub>: A New Direct-Gap Semiconductor. *Phys. Rev. Lett.* **2010**, *105*, 136805.
- Xiao, D.; Liu, G.-B.; Feng, W.; Xu, X.; Yao, W. Coupled Spin and Valley Physics in Monolayers of MoS<sub>2</sub> and Other Group-VI Dichalcogenides. *Phys. Rev. Lett.* **2012**, *108*, 196802.
- Cao, T.; Wang, G.; Han, W.; Ye, H.; Zhu, C.; Shi, J.; Niu, Q.; Tan, P.; Wang, E.; Liu, B.; Feng, J. Valley-Selective Circular Dichroism of Monolayer Molybdenum Disulphide. *Nat. Commun.* **2012**, *3*, 887.
- Zeng, H.; Dai, J.; Yao, W.; Xiao, D.; Cui, X. Valley Polarization in MoS<sub>2</sub> Monolayers by Optical Pumping. *Nat. Nanotechnol.* **2012**, *7*, 490–493.
- Mak, K. F.; He, K.; Shan, J.; Heinz, T. F. Control of Valley Polarization in Monolayer MoS<sub>2</sub> by Optical Helicity. *Nat. Nanotechnol.* **2012**, *7*, 494–498.
- Zeng, H.; Liu, G.-B.; Dai, J.; Yan, Y.; Zhu, B.; He, R.; Xie, L.; Xu, S.; Chen, X.; Yao, W.; Cui, X. Optical Signature of Symmetry Variations and Spin-Valley Coupling in Atomically Thin Tungsten Dichalcogenides. *Sci. Rep.* **2013**, *3*, 1608.
- Kumar, N.; Najmaei, S.; Cui, Q.; Ceballos, F.; Ajayan, P. M.; Lou, J.; Zhao, H. Second Harmonic Microscopy of Monolayer MoS<sub>2</sub>. *Phys. Rev. B* **2013**, *87*, 161403(R).
- Malard, L. M.; Alencar, T. V.; Barboza, A. P. M.; Mak, K. F.; de Paula, A. M. Observation of Intense Second Harmonic Generation from MoS<sub>2</sub> Atomic Crystals. *Phys. Rev. B* **2013**, *87*, 201401(R).
- Li, Y.; Rao, Y.; Mak, K. F.; You, Y.; Wang, S.; Dean, C. R.; Heinz, T. F. Probing Symmetry Properties of Few-Layer MoS<sub>2</sub> and h-BN by Optical Second-Harmonic Generation. *Nano Lett.* **2013**, *13*, 3329–3333.

11. Kim, C.-J.; Brown, L.; Graham, M. W.; Hovden, R.; Havener, R. W.; McEuen, P. L.; Muller, D. A.; Park, J. Stacking Order Dependent Second Harmonic Generation and Topological Defects in h-BN Bilayers. *Nano Lett.* **2013**, *13*, 5660–5665.
12. Li, G.; Luican, A.; Lopes dos Santos, J. M. B.; Castro Neto, A. H.; Reina, A.; Kong, J.; Andrei, E. Y. Observation of Van Hove Singularities in Twisted Graphene Layers. *Nat. Phys.* **2010**, *6*, 109–113.
13. Havener, R. W.; Zhuang, H.; Brown, L.; Hennig, R. G.; Park, J. Angle-Resolved Raman Imaging of Interlayer Rotations and Interactions in Twisted Bilayer Graphene. *Nano Lett.* **2012**, *12*, 3162–3167.
14. Kim, K.; Coh, S.; Tan, L. Z.; Regan, W.; Yuk, J. M.; Chatterjee, E.; Crommie, M. F.; Cohen, M. L.; Louie, S. G.; Zettl, A. Raman Spectroscopy Study of Rotated Double-Layer Graphene: Misorientation-Angle Dependence of Electronic Structure. *Phys. Rev. Lett.* **2012**, *108*, 246103.
15. Ponomarenko, L. A.; Gorbachev, R. V.; Yu, G. L.; Elias, D. C.; Jalil, R.; Patel, A. A.; Mishchenko, A.; Mayorov, A. S.; Woods, C. R.; Wallbank, J. R.; *et al.* Cloning of Dirac Fermions in Graphene Superlattices. *Nature* **2013**, *497*, 594–597.
16. Geim, A. K.; Grigorieva, I. V. Van der Waals Heterostructures. *Nature* **2013**, *499*, 419–425.
17. Britnell, L.; Ribeiro, R. M.; Eckmann, A.; Jalil, R.; Belle, B. D.; Mishchenko, A.; Kim, Y.-J.; Gorbachev, R. V.; Georgiou, T.; Morozov, S. V.; *et al.* Strong Light-Matter Interactions in Heterostructures of Atomically Thin Films. *Science* **2013**, *340*, 1311–1314.
18. Britnell, L.; Gorbachev, R. V.; Jalil, R.; Belle, B. D.; Schedin, F.; Mishchenko, A.; Georgiou, T.; Katsnelson, M. I.; Eaves, L.; Morozov, S. V.; *et al.* Field-Effect Tunneling Transistor Based on Vertical Graphene Heterostructures. *Science* **2012**, *335*, 947–950.
19. Terrones, H.; López-Urías, F.; Terrones, M. Novel Hetero-Layered Materials with Tunable Direct Band Gaps by Sandwiching Different Metal Disulfides and Diselenides. *Sci. Rep.* **2013**, *3*, 1549.
20. Kou, L.; Frauenheim, T.; Chen, C. Nanoscale Multilayer Transition-Metal Dichalcogenide Heterostructures: Band Gap Modulation by Interfacial Strain and Spontaneous Polarization. *J. Phys. Chem. Lett.* **2013**, *4*, 1730–1736.
21. Lee, Y.-H.; Zhang, X.-Q.; Zhang, W.; Chang, M.-T.; Lin, C.-T.; Chang, K.-D.; Yu, Y.-C.; Wang, J. T.-W.; Chang, C.-S.; Li, L.-J.; *et al.* Synthesis of Large-Area MoS<sub>2</sub> Atomic Layers with Chemical Vapor Deposition. *Adv. Mater.* **2012**, *24*, 2320–2325.
22. Boyd, R. *Nonlinear Optics*; Academic Press: London, 2008.
23. Beal, A. R.; Hughes, H. P. Kramers-Krönig Analysis of the Reflectivity Spectra of 2H-MoS<sub>2</sub>, 2H-MoSe<sub>2</sub> and 2H-MoTe<sub>2</sub>. *J. Phys. C: Solid State Phys.* **1979**, *12*, 881–890.
24. Lee, Y.-H.; Yu, L.; Wang, H.; Fang, W.; Ling, X.; Shi, Y.; Lin, C.-T.; Huang, J.-K.; Chang, M.-T.; Chang, C.-S.; *et al.* Synthesis and Transfer of Single-Layer Transition Metal Disulfides on Diverse Surfaces. *Nano Lett.* **2013**, *13*, 1852–1857.
25. Huang, J.-K.; Pu, J.; Hsu, C.-L.; Chiu, M.-H.; Juang, Z.-Y.; Chang, Y.-H.; Chang, W.-H.; Iwasa, Y.; Takenobu, T.; Li, L.-J. Large-Area Synthesis of Highly Crystalline WSe<sub>2</sub> Monolayers and Device Applications. *ACS Nano* **2014**, *8*, 923–930.
26. Zhang, W.; Chuu, C.-P.; Huang, J.-K.; Chen, C.-H.; Tsai, M.-L.; Chang, Y.-H.; Liang, C.-T.; Chen, Y.-Z.; Chueh, Y.-L.; He, J.-H.; *et al.* Ultrahigh-Gain Photodetectors Based on Atomically Thin Graphene-MoS<sub>2</sub> Heterostructures. *Sci. Rep.* **2014**, *4*, 3826.